Tidal Response and Shape of Hot Jupiters

SEAN M. WAHL D, 1 DANIEL THORNGREN D, 2,3 TIGER LU D, 4 AND BURKHARD MILITZER D, 5

Department of Earth and Planetary Science, University of California, Berkeley, CA 94720, USA
 Department of Physics, University of California, Santa Cruz
 Institute for Research on Exoplanets, Université de Montréal, Canada
 Astronomy Department, California Institute of Technology, Pasadena, California 91125, USA.
 Department of Astronomy, University of California, Berkeley, CA 94720, USA

ABSTRACT

We study the response of hot Jupiters to a static tidal perturbation using the Concentric MacLaurin Spheroid (CMS) method. For strongly irradiated planets, we first performed radiative transfer calculations to relate the planet's equilibrium temperature, T_{eq} , to its interior entropy. We then determined the gravity harmonics, shape, moment of inertia, and the static Love numbers for a range of two-layer interior models that assume a rocky core plus a homogeneous and isentropic envelope composed of hydrogen, helium, and heavier elements. We identify general trends and then study HAT-P-13b, the WASP planets 4b, 12b, 18b, 103b, and 121b, as well as Kepler-75b and CoRot-3b. We compute the Love numbers, k_{nm} , and transit radius correction, ΔR , which we compare with predictions in the literature. We find that the Love number, k_{22} , of tidally locked giant planets cannot exceed the value 0.6, and that the high $T_{\rm eq}$ consistent with strongly irradiated hot Jupiters tend to further lower k_{22} . While most tidally locked planets are well described by a linear-regime response of $k_{22} = 3J_2/q_0$ (where q_0 is the rotation parameter of the gravitational potential), for extreme cases such as WASP-12b, WASP-103b and WASP-121b, nonlinear effects can account for over 10% of the predicted k_{22} . k_{22} values larger than 0.6, as they have been reported for planets WASP-4b and HAT-P13B, cannot result from a static tidal response without extremely rapid rotation, and thus are inconsistent with their expected tidally-locked state.

Keywords: Exoplanets — Hot Jupiters — Tides

1. INTRODUCTION

In this paper, we study the response of rotating giant exoplanets to tidal perturbations using the nonperturbative Concentric MacLaurin Spheroid (CMS) method (Hubbard 2013). The shape of a fluid planet results from a balance of tidal interactions with other celestial bodies and the planets' rotation with self-gravity from the planets' interior mass distribution. While the gas giant planets in our solar system, Jupiter and Saturn, have had their interiors probed by precise spacecraft gravity measurements (Folkner et al. 2017; Iess et al. 2019), the tremendous distance to exoplanets necessitates more indirect means for studying their interiors. A class of exoplanets that is well suited for the study of tidal interactions is the hot Jupiters, whose relatively large masses and close-in orbits with their host star lead to much stronger tidal interactions than for any planet in our solar system. In addition, intense insolation allows their interiors to maintain much

of their primordial heat, with equilibrium temperature, $T_{\rm eq} > 1000$ K (Miller & Fortney 2011), leading to their well-documented, inflated gaseous envelopes (Charbonneau et al. 2000; Henry et al. 2000; Guillot & Showman 2002), which are even more prone to deformation by tidal interactions than colder planets.

The deformation of a planet can be characterized by the shape of its observable surface, via ratios radii along the of principle axes, a, b and c, or through normalized moments of its gravity field. For tidal interactions in particular, the first order response is conventionally reported as the second-degree fluid Love number k_{22} (Love 1909).

Batygin et al. (2009) identified a means of constraining k_{22} for HAT-P-13b by considering its special orbital configuration with a highly eccentric outer companion planet. Buhler et al. (2016) applied this technique using observations of secondary eclipses to measure the eccentricity, e, and found a $k_{22} = 0.31^{+0.08}_{-0.05}$. Mean-

while, Hardy et al. (2017) used independent observations of HAT-P-13b secondary eclipses and inferred a much larger value of $k_{22} = 0.81 \pm 0.10$. Ragozzine & Wolf (2009) put forward another method for measuring k_{22} by relating it to apsidal precession, which can manifest itself as transit timing variations (TTV) between temporally separated transit observations. This method was applied to WASP-4b by Bouma et al. (2019) who estimated a $k_{22} = 1.20^{+0.20}_{-0.26}$ from TESS observations showing an offset in transit time with respect to predictions based on observations stretching back to 2007. Likewise, Csizmadia et al. (2019) estimated $k_{22} = 0.62^{+0.55}_{-0.19}$ for WASP-18b using a similar technique, but with apsidal precession rate inferred radial velocity variations (RV) instead. An initial suggestion of a detection of apsidal precision for WASP 12-b was ruled out by Campo et al. (2011).

The shape of the observable surface of a sufficiently nonspherical planet can be inferred from transit light curves for both fast-rotating oblate planets (Seager & Hui 2002) and tidally-elongated, prolate planets (Leconte et al. 2011; Burton et al. 2014). With the exception of special-case interactions with asecondary companion planet, most close-in hot Jupiters are expected to have evolved to a tidally-locked state with negligible eccentricity (Lin & Gu 2004; Jackson et al. 2008). Because tidal locking limits the rotation rate to match the orbital period, the tidally induce prolateness is generally more pronounced than the rotational oblateness. For sufficiently close-in hot Jupiters this can lead to a systematic underestimation of reported planetary radius and, by consequence, and overestimation of the bulk density. The effects of rotation and tidal perturbation were analyzed in detail by Leconte et al. (2011) who derived a predictive theory how to correct the observed radii. We will compare our prediction of the radius correction of WASP-12b with their work. Correia (2014) formulated an analytical shape model with an assumed ellipsoidal shape, and a tidal response following the Darwin-Radau equation and calculated a, b and c for a number of hot Jupiters, including WASP-4b, WASP-12b, WASP19b and WASP-103b. Akinsanmi et al. (2019) applied the Correia's shape model to a predict the number of transits required to constrain the shape Love number h_2 of WASP-103b and WASP-121b for the TESS, PLATO and JWST spacecraft. Similarly, Hellard et al. (2019) and Hellard et al. (2020) predicted the sensitivity of a number of spacecraft, including TESS, PLATO and JWST, to measuring k_{22} for Wasp-121b.

There is extensive literature on the theory of calculating the shape of a liquid planet, dating back over a cen-

tury (H. & Jeans 1920), with pioneering calculations on giant planets presented in Gavrilov & Zharkov (1977). The most commonly used method, known as the theory of figures (Zharkov & Trubitsyn 1978), uses a perturbative approach to determine the planet's response to small deviations of the potential from spherical symmetry. Other works have extended the theory of figures to consider second order effects through higher order perturbative theory (Zharkov 2004; Zharkov & Gudkova 2010; Correia & Rodríguez 2013). Padovan et al. (2018) adapted a related perturbative method using a matrix-propagator approach, more common in geophysical applications, to exoplanets.

Hubbard (2013) introduced the concentric Maclaurin spheroid (CMS) technique, an nonperturbative, iterative method for more precise calculations of selfconsistent shape and gravitational field. The CMS method was subsequently extended to three dimensions and applied to the cases of Jupiter and Saturn (Wahl et al. 2016, 2017a; Nettelmann 2019; Wahl et al. 2020). In this work we apply the CMS method to hot Jupiter exoplanets for the first time. While more computationally expensive than the theory of figures, the CMS method correctly accounts for non-linear effects that become relevant for extremely deformed planets, most notably effects on the order of the product of rotational and tidal perturbations (Wahl et al. 2017a). These nonlinear effects lead to a splitting of the static k_{nm} with degree m, and an enhancement of k_{22} that is significant for Jupiter and Saturn (Lainey et al. 2017, 2020; Durante et al. 2020; Wahl et al. 2020).

In addition to the numerical technique, models of shape and gravity also depend on the assumed interior structure and the hydrogen-helium equation of state (EOS). The relationship between tidal response and core mass is discussed in numerous works, (e.g. Batygin et al. 2009; Ragozzine & Wolf 2009), with more centrally concentrated density distributions leading to smaller values of k_{22} . Many studies of giant planet interiors employ the semi-empirical Saumon et al. (1995b) EOS, while more recent studies have considered equations of state fit to ab-initio molecular dynamics simulations of hydrogen-helium mixtures based on density functional theory (DFT-MD) (Militzer & Hubbard 2013; Becker et al. 2015; Chabrier et al. 2019), while some theoretical works consider the simpler, more analytically tractable polytropic EOS, (e.g. Leconte et al. 2011). The most pronounced difference between DFT-MD bases equations and Saumon et al. (1995b) occurs at pressures of ~ 100 GPa; as hydrogen transitions from a molecular insulator to an atomic metal (Vorberger et al. 2010), DFT-MD predicts adiabatic temperature profiles that are are

cooler and denser. Kramm et al. (2012) explored the possible interior structure of giant planet, HAT-P13b using interior models with the Saumon et al. (1995b) EOS and the theory of figures to calculate Love number, k_{22} . Becker et al. (2018) calculated Love numbers using a DFT-MD EOS and the theory of figures for two giant exoplanets Kepler-75b (formerly KOI-889b) and Corot-3b. A similar study of planets in the super-Earth exoplanet regime was carried out by Kellermann et al. (2018).

2. METHODS

We first solve the equations of hydrostatic equilibrium for a nonrotating planet as described in Seager et al. (2007). For the EOS of hydrogen-helium mixtures, we adopt the results from Militzer & Hubbard (2013), who employed density functional theory molecular dynamics (DFT-MD) simulations to derive an EOS table with absolute entropies at pressure higher than ~ 5 GPa. At lower pressure, we use the Saumon-Chabrier EOS that was derived with semi-analytical methods (Saumon et al. 1995a). Heavier elements are incorporated into the H-He mixture by following approach in Hubbard & Militzer (2016a). For the core, we adopted a terrestrial iron-rock ratio of 0.325. For simplicity, we assumed both components are homogeneously mixed. The silicates are described as in Seager et al. (2007). For iron, we employed results from DFT-MD simulations (Wilson & Militzer 2014).

For all calculations, we assume a protosolar value for the helium mass fraction, Y, of the envelope by setting Y/(1-Z) = 0.27774 (Lodders 2010). The fraction of heavy elements, Z, and the entropy, S, of the are input parameters of our simulations, which govern the density structure of the hydrogen-helium envelope. We provide entropy values in units of Boltzmann constant per electron (k_B/el) , which is referenced to an atomic H:He ratio of 110:9 from Militzer & Hubbard (2013). In these units, helium rain is predicted to start at $S = 7.2 k_B/el$, the maximum entropy for which the interior adiabat intersects the pressure-temperature region in Fig. 1, in which hydrogen and helium are predicted to become immiscible Morales et al. (2010) because hydrogen transitions from an insulating, molecular states to an atomic, metallic fluid (Vorberger et al. 2010) while helium remains in an insulating state. In this work, however, we are primarily concerned with hot Jupiters that we assume to have homogeneously mixed envelopes with entropies $S \ge 7.2 \ k_B/\text{el}$.

In addition to the S and Z values for the envelope, adopt values for masses the core and envelope (see Tab. 1). We integrate the equations of hydrostatic equi-

librium starting from a central pressure, P_c , to outer pressure boundary, set to 1 bar, where we assume envelope becomes transparent. We iterate over different P_c values to match the total mass of the planet. In cases for which we have a radius measurement, we iterate over of the core mass or envelope Z to match the planet's mass and radius simultaneously.

The planet mass, M, and volumetric average radius, a_0 , from our calculations of nonrotating planets define the planetary units of mass and length for all following CMS calculations rotating and tidally perturbed planets. In absence of a tidal perturbation, we express the gravitational potential of a axisymmetric rotating planet.

$$V(r,\mu) = \frac{GM}{r} \left[1 - \sum_{n=1}^{\infty} \left(\frac{a_0}{r} \right)^{2n} J_{2n} P_{2n}(\mu) \right] , \quad (1)$$

in terms of the gravity harmonics,

$$J_n = -\frac{2\pi}{Ma_0^n} \int_{-1}^{+1} d\mu \int_{0}^{r_{\text{max}}(\mu)} dr \ r^{n+2} \ P_n(\mu) \ \rho(r,\mu) \quad . \quad (2)$$

 $r_{\rm max}$ defines the outer surface of the planet as function of $\mu = \cos(\theta)$ with θ being the polar angle. P_n are the Legendre polynomials and G is the gravitational constant. We also define two rotational parameters,

$$q_0 = \frac{\omega^2 a_0^3}{GM}$$
 and $q_e = \frac{\omega^2 a_e^3}{GM}$, (3)

where ω is the angular frequency of the planet's assumed solid-body rotation. $q_{\rm e}$ is often invoked in the literature when specific planets are discussed for which the equatorial radius, $a_{\rm e}$, is known while a_0 is not. For the purposes of this paper, q_0 is more convenient because it does not depend on ω or the equatorial radius, which will only become known once the CMS calculation has converged.

The CMS technique (Hubbard 2013) is a nonperturbative method for deriving the shape and interior structure of rotating planets in hydrostatic equilibrium. Typically one keeps the equatorial radius constant and adjusts the core mass or Z of the envelop to match the observed mass of the planet (e.g. Hubbard & Militzer 2016b). This approach does not serve our needs because, for different rotation rates, we wish to study what shape is assumed by a planet of given core and envelop masses. The equatorial radii of the planet (and that of the core) are results, not input parameters, of such a calculation. Hubbard (2013) introduced a grid of λ points, normalized radii from the planet's center to the equator that anchor the equatorial points of all the equipotential surfaces as the CMS converges towards a self-consistent hydrostatic solution. Here we work with two λ grid, one

Planet mass M $[M_J]$	Input parameter					
Core mass M_c $[M_{\oplus}]$	Input parameter. Sets the envelope mass to $M-M_c$. Core shape and radius are derived.					
Entropy of envelope S [k_B /el.]	Input parameter chosen between 7.2 and 12.0. Sets the temperature-pressure profile of the envelope in Fig. 1. Is derived from $T_{\rm eq}$.					
Mass fraction of heavy elements in envelope Z	Input parameter that sets also the mass fractions of hydrogen, $X = 1 - Y - Z$, and helium $Y = 0.27774 \times (1 - Z)$ because we assume a protosolar helium abundance (Lodders 2010).					
Planet radius a_0 [R _J]	Derived in calculations of nonrotating planet. Alternatively, Z or M_c can be adjusted to match a certain radius.					

Table 1. Parameters of our two-layer interior models.

for the core and one for the envelope. Following Militzer et al. (2019), for the jth spheroid surface, λ_i is chosen so that a logarithmic grid in density emerges $(\rho(\lambda_i)/\rho(\lambda_{i+1}) = \text{const.})$. We determine the $\rho(\lambda)$ relation from a nonrotating planet calculation, which we then employ for the subsequent calculations with rotation and tides. The density variations throughout core and envelope determine how many grid points must be invested into representing each region accurately. We used 1025 layers in our reported CMS calculations, but already even with 129 layers one obtains good results. For example, for a WASP-12b model with a $0.29 \,\mathrm{M}_J$ core and $129 \,\mathrm{M}_J$ layers, we calculate the Love number $k_{22}=0.16258843$ and transit radius correction, ΔR =0.034046. With 1025 layers, we derived $k_{22}=0.16483250$ and $\Delta R=0.031489$, which are both fairly similar. As we will demonstrate, these deviations are small compared to those resulting from changes model assumptions and planet parameters.

In order to match the core and envelope masses in our CMS calculations of rotating planets, we rescale the λ grids of the core and envelope separately as the CMS method converges to a hydrostatic solution. This poses no technical challenges unless the planets are rotating extremely fast $(q_0 \gtrsim 0.3)$.

Once this axisymmetric CMS calculation has converged, we study the planet's shape, compute the gravity harmonics J_n , and derive the moment of inertia, $C/(Ma_0^2)$. The hydrostatic structure of axisymmetric CMS calculation also serves as input for a 3D CMS calculation that studies the static tidal response to an external perturber, which could be a the planet's host star, a satellite or a companion planet.

The CMS technique was extended to three dimensions by Wahl et al. (2017a). In this version, a third potential term, the gravitational potential from a perturbing mass, m_S at distance, \mathbf{R} , from the planet's center of mass,

$$W(\mathbf{r}, \mathbf{R}) = \frac{Gm_S}{|\mathbf{R} - \mathbf{r}|},\tag{4}$$

is added to Eqn. 1, and equipotential surfaces for the combined potential are evaluated on a 3D grid $\mathbf{r}(r, \mu, \phi)$. Wahl et al. (2020) updated the 3D CMS method by modifying W by subtracting out a linear term determined by an average force.

$$\tilde{W}(\mathbf{r}, \mathbf{R}) = W(\mathbf{r}, \mathbf{R}) - \langle \mathbf{F} \rangle \cdot \mathbf{r}.$$
 (5)

This enforces the constraint that the planet's center of mass remains at a specified distance from the perturber. This procedure avoids an issue where the precision of the converged solution is limited by a small shift in center of mass that must be removed each iteration (Wahl et al. 2016, 2017a).

As with the rotational parameter, we can define two tidal parameters,

$$q_{\rm tid,0} = -3 \frac{m_S a_0^3}{M R^3}$$
 and $q_{\rm tid,e} = -3 \frac{m_S a_{\rm e}^3}{M R^3}$, (6)

where m_S is the mass of the perturber (the stellar mass for the purposes of this study), and R is the distance to the perturber, in our case the orbital distance. We once again elect to use $q_{\rm tid,0}$ for convenience and refer to simply as $q_{\rm tid}$ for the remainder of the paper. The third and final governing parameter for the tidal calculation is simply the ratio of the planet's radius to the orbital radius, a_0/R . In our own solar system, the rapid rotation Jupiter and Saturn place them in the regime where $q_0 \gg |q_{\rm tid}|$, even for their strongest perturbers, Io and Tethys respectively. In contrast, tidally-locked hot Jupiters typically have values of $q_{\rm tid}$ is of a similar or greater magnitude than q_0 .

As in the axisymmetric case, the converged equipotential surfaces define a density structure from which gravitational field strength can be integrated, now in terms of the tesseral gravity moments C_{nm} and S_{nm} (Wahl et al. 2017b). For simplicity, we assume that the perturber is in the planet's equatorial plane with $\mu = \cos \theta = 0$. For an exoplanet-star system, this corresponds to a planet with zero obliquity. While this is not a good approximation for the exoplanet population

as a whole, it is likely to be the case for many closein hot Jupiters (Lin & Gu 2004; Jackson et al. 2008). We further simplify the geometry by defining the coordinate system such that the perturber is at $\phi = 0$, which by symmetry requires $S_{nm} = 0$. The tidal Love number can then be expressed as (Gavrilov & Zharkov 1977; Zharkov & Trubitsyn 1978),

$$k_{nm} = -\frac{2}{3} \frac{(n+m)!}{(n-m)!} \frac{C_{nm}}{P_n^m(0)q_{\text{tid }0}} \left(\frac{a_0}{R}\right)^{2-n}, \quad (7)$$

where $P_n^m(0)$ is the associated Legendre polynomial evaluated at $\mu = 0$. For a distant perturber, the m=2 moment dominates the expansion, but higher order moments become more significant as a_0/R increases. We note that the Jupiter and Saturn k_{22} reported later for comparison defined k_{nm} with $q_{\rm tid,e}$ instead of $q_{\rm tid,0}$ (Wahl et al. 2017a, 2020).

In the absence of rotation, k_{nm} is degenerate with respect to m. By contrast, rapidly rotating planets, such as Jupiter an Saturn, are predicted to have have significant splitting of love numbers of the same order n (Wahl et al. 2016, 2017a, 2020). The most readily observable manifestation of this is an enhancement of k_{22} compared to a nonrotating analogue planet, which is evident for observations of both Jupiter (Durante et al. 2020) and Saturn (Lainey et al. 2017, 2020).

3. RESULTS AND DISCUSSION

3.1. General trends

In Fig. 2, we compare the gravity harmonics of four Saturn-mass planets with 10 Earth mass (M_{\oplus}) cores as function of the rotational parameter, q_0 . By definition, all curves start from $J_0 = -1$. All cases decay exponentially with increasing degree, n, but their decay rates vary with the magnitude of q_0 . For slowly rotating planets, the J_n decay most rapidly, which is consistent with the fact that all $J_{n>2}$ are zero for a nonrotating planet. With increasing degree, the weight functions of the gravity coefficients become more sharply peaked near the surface (Militzer et al. 2016). This means the J_n decay more rapidly for a hot, puffy planet ($S=11 k_b/el$) that has less mass near the surface. It also implies that the J_n decay more slowly for fast rotating planets, for which the centrifugal force shifts more mass towards the equator.

In Fig. 3, we compare various properties of a cold and hot Saturn-mass planet $(S = 7.2 \text{ and } 11.0 \text{ } k_b/\text{el})$ as well as a cold Jupiter-mass planet $(S = 7.2 \text{ } k_b/\text{el})$ each with a $10 \text{ } M_{\oplus}$ core. For moderate values of q_0 , we find the gravity harmonics, J_2 , J_4 , and J_6 scale approximately as q_0 , q_0^2 , as q_0^3 , respectively, because with increasing q_0 , additional mass is shifted towards the equator. For all

three planets, we find a sizeable increase in the equatorial radius for large q_0 . However, the polar radius only shrinks significantly for the two colder planets. The hot Saturn-mass planet is so inflated $(a_0 = 2.6 \, R_J)$ and the centrifugal force as large for high q_0 that polar radius hardly shrinks as the equatorial radius increases.

In the bottom panel of Fig. 3, we plot the moment of inertia. For the hot, puffy Saturn-mass planet, it hardly changes over q_0 interval from 0 to 0.25. For the two colder planets, we see a modest increase in the moment of inertia for $q_0 > 0.1$ as the centrifugal force distributes more mass away from the axis of rotation.

The Darwin-Radau relation gives an approximate expression for the moment of inertia, C, of slowly rotating planets (see discussion in Zharkov & Trubitsyn 1978),

$$\frac{C}{Ma_{\rm e}^2} = \frac{2}{3} \left(1 - \frac{2}{5} \sqrt{x} \right) \tag{8}$$

$$x_1 = 1 + \eta \quad \text{with} \quad \eta = \frac{5}{2} \frac{q_{\rm e}}{f} \quad \text{and} \quad f = \frac{a_{\rm e} - c}{a_{\rm e}}$$

$$x_2 = \frac{5q_s}{3J_2 + q_s} - 1 \quad \text{with} \quad q_s = \frac{\omega^2 s^3}{GM} = q_{\rm e} \frac{s^3}{a_{\rm e}^3} .$$

where $a_{\rm e}$, c, and s are the equatorial, polar, and sphericalized radii. $(\frac{4}{3}\pi s^3)$ equals the planet volume.) The quantity x can either be derived from the oblateness, f, or expressed in terms of the parameters J_2 and q_s . Both expressions give similar results unless the density contrast between core and envelope is too large, as we see for the hot Saturn-mass planet in Fig. 3. In this case, both Darwin-Radau expressions overestimate the moment of inertia by $\sim 50\%$ even in the limit of a slowly rotating planet. In this limit, Darwin-Radau results agree fairly well with the CMS predictions of the colder Saturn- and Jupiter-mass planets. The equatorial radii of these two planets are 0.88 and 1.0 R_J while the hot Saturn-mass planet is significantly inflated $(a = 2.6 R_J)$, which explains the break-down of the Darwin-Radau expression. Furthermore, one should also be cautious in applying the Darwin-Radau approximation to fast rotating planets like Saturn and Jupiter, with $q_{\rm e}=0.158$ and 0.0892respectively. In this case, q_e is no longer a small parameter and the Darwin-Radau assumptions break down.

In Fig. 4, we compare the Love numbers, k_{nm} , of six planets: three masses 0.3, 1.0, and 10.0 M_J and cold and hot $(S=7.2 \text{ and } 11.0 \text{ } k_b/\text{el})$ interiors. All have 10 M_{\oplus} cores. In the limit of slow rotation, for given n, we find that non-zero k_{nm} values of any m all approach a common value, as expected since angular dependence disappears for a nonrotating. All Love number rise with increasing rotation rate. However, this rise is very small for the hot Saturn-mass planets, which exhibit the smallest Love numbers, followed by the hot Jupiter-mass

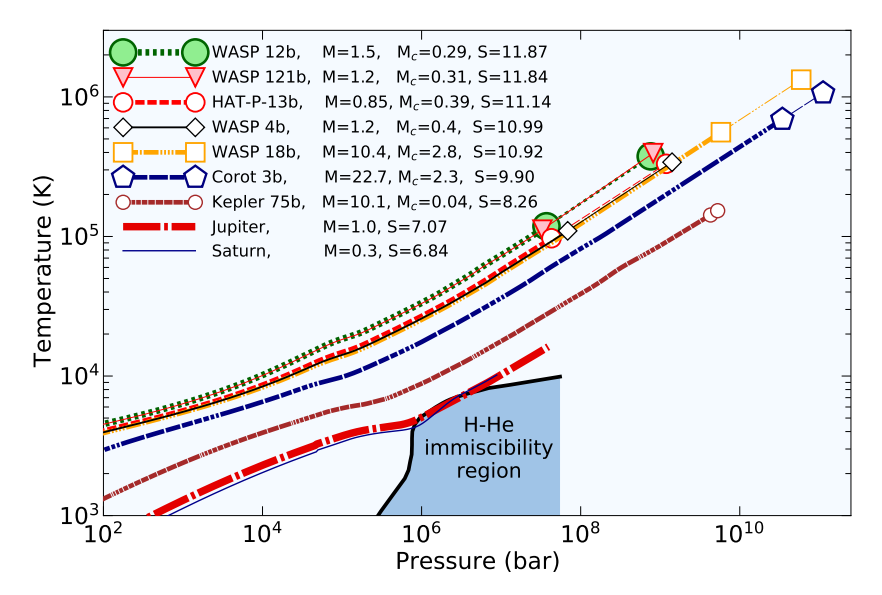


Figure 1. Pressure-temperature conditions in the deep interiors of selected planets. Masses of planets, M, and their cores, M_c , are given in Jupiter masses in the legend. The two symbols bracket conditions within the planet cores, from the core-envelope boundary (lower left) to the very center (upper right). The distance between the two symbols is primarily controlled by the ratio M_c/M . The entropy of the envelope is give in units of k_b/el in the legend. Adiabats with $S \leq 7.2$ k_b/el intersect the hydrogen-helium immiscibility region (Morales et al. 2010).

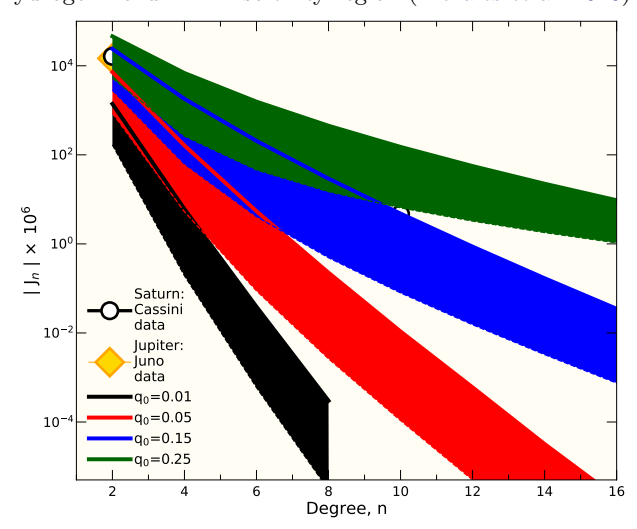


Figure 2. Decay of the gravity harmonics with increasing degree, n, is shown for Saturn-mass planets that rotate at different rates. The thick solid lines and thin dashes lines correspond to cold ($S=7.2~k_b/\mathrm{el}$) and hot ($S=11.0~k_b/\mathrm{el}$) planets respectively. Spacecraft measurements of Jupiter and Saturn have been included for comparison. The unexpectedly large values of Saturn's J_6 , J_8 , and J_{10} have been attributed to differential rotation (Iess et al. 2019), which we do not include in our exoplanet models because there are no observations to constrain the winds on these planets.

planet. On the other hand, the cold Jupiter-mass planet exhibits the largest Love numbers of all six planets, except for very large q_0 values where the cold 10 Jupiter-mass planet shows a larger response. For the hot plan-

ets (S=11 k_b /el), the Love number increases with rising planet mass while no simple trend appears for three colder planets.

In Fig. 5, we compare the Love number, k_{22} , as function of various parameters in order to motivate $k_{22}\approx 0.6$ as a plausible maximum for slowly rotating planets. In the upper panel, we study the dependence on planet mass. For a cold planets $(S=7.2~k_b/{\rm el}),~k_{22}$ assumes a maximum value of 0.603 for a one Jupiter-mass planet. This planet has a radius of $1.026~R_J$, which is close to the maximal radius of $1.069~R_J$ that emerges for three Jupiter mass planet.

In the middle panel, we plot k_{22} as function of the envelope entropy, S. With increasing S, the envelope becomes less dense and thus shows a reduced tidal response. When the entropy of a one Jupiter-mass planet is reduced from S=7.2 to a 6.84 k_b/el , a typical value for Saturn, k_{22} increases from 0.603 to 0.618. Since this represent cold planet, we argue 0.6 is still a reasonable upper bound for k_{22} of slowly rotating hot Jupiters.

In the lower panel, we study the dependence of k_{22} as a function of core mass fraction while keeping the total planet mass fixed at 1.0 and 10.0 M_J . As expected, k_{22} decreases with increasing core mass fractions because it concentrates more mass in the planet's center where is responds less to tidal perturbations. It is this dependence of k_{22} on core mass that will enable inference of an exoplanet's core mass with future transit measurements (e.g. Batygin et al. 2009; Ragozzine & Wolf 2009).

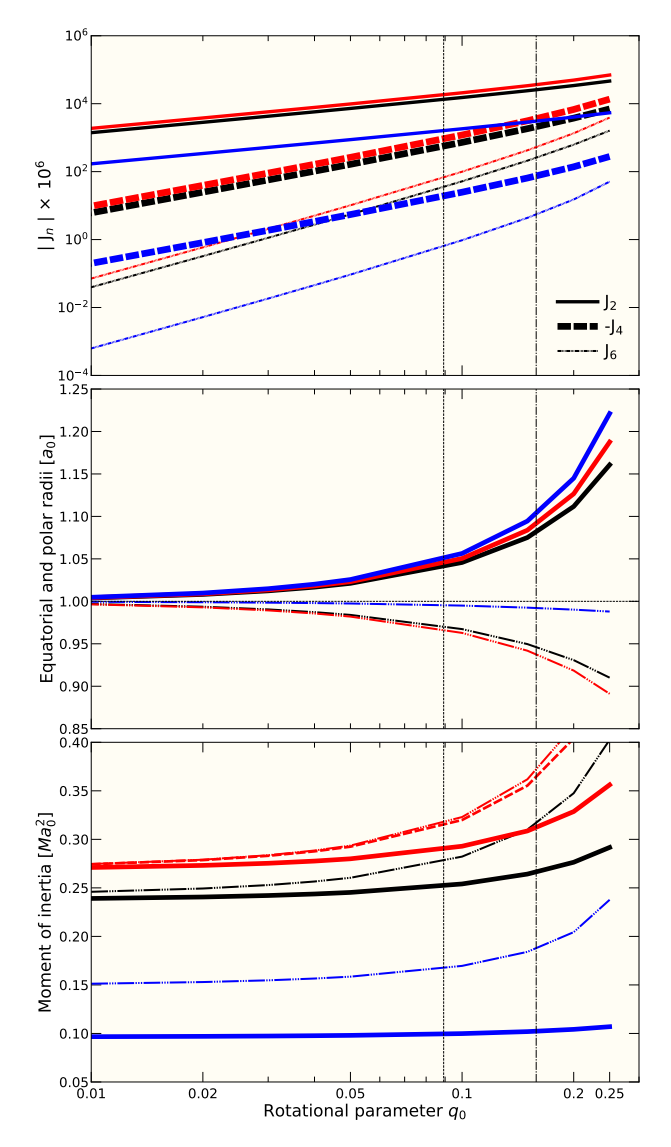


Figure 3. Models of three rotating planets without tidal perturbations: cold (S=7.2, black, $a_0 = 0.876 R_J$) and hot $(S=11.0 \ k_b/el, red, a_0 = 2.604 R_J)$ Saturn-mass planet as well as a cold Jupiter-mass planet (S=7.2 k_b/el , blue, $a_0 = 1.004 R_J$) are compared as function of q_0 . The vertical dashed and dash-dotted lines mark the q_e values of Jupiter and Saturn respectively. The upper panel shows the gravity harmonics J_2 , J_4 , and J_6 that scale like q_0 , q_0^2 , and q_0^3 for small q_0 values. The middle panel shows how the equatorial (solid) and polar (dash-dotted lines) radii of these planets change with increasing rotation rate. The radii of the nonrotating planets, a_0 , are used as normalization. In the lower panel, we compare the CMS predictions (solid lines) for the normalized moment of inertia with the Darwin-Radau expressions: one involving J_2 (Eq. (9), dash-dotted line) and the other relying on the oblateness (Eq. (8), dotted line).

3.2. Results for selected exoplanets

Meaningful models of the interior structure of a given planet require constraints on both planetary mass and radius, which are determined by independent observation techniques. Table 2 summarizes the input parameters for eight exoplanets considered here. Three of the selected planets, HAT-P-13b (Buhler et al. 2016; Hardy et al. 2017), WASP-18b (Csizmadia et al. 2019) and WASP-4b (Bouma et al. 2019) have reported observational constraints on k_{22} , while WASP-12b (Campo et al. 2011), WASP-103b (Akinsanmi et al. 2019) and WASP-121b (Hellard et al. 2020) have each been invoked in studies of the detectibility of k_{22} . Figure 6 shows reported k_{22} observations compared to the limits on k_{22} we find for all eight selected exoplanets.

Modelling a realistic interior structure of a giant planet necessarily involves calculating its thermal structure. For the two-layer models considered, it is natural to parameterize this in terms of the specific entropy of the envelope, S. Cool giant planets like Jupiter and Saturn begin their life with a high specific entropy (from their formation heat) and gradually cool over time (Fortney et al. 2007, e.g). Giant planets whose incident flux exceed 2×10^8 erg / s / cm², however, exhibit large radii indicative of hotter interiors than is expected from the physical processes seen in their cooler cousins (Miller & Fortney 2011; Demory & Seager 2011).

This hot Jupiter inflation effect may be modeled as an additional heat source within the planet which varies with the incident stellar flux (Thorngren & Fortney 2018; Sarkis et al. 2021). As they evolve, these planets will, therefore, approach a steady state where the energy flux out of the interior (parameterized by the intrinsic temperature $T_{\rm int}$) is equal to the anomalous heating (Thorngren et al. 2019). Using the atmosphere models of Fortney et al. (2009), we can relate the envelope's specific entropy to $T_{\rm int}$. Then we apply the results of Thorngren & Fortney (2018), which relate the anomalous heating to the incident flux. The final product is a relationship between the specific entropy of the planet with the incident flux onto the planet (Fig. 7). This is helpful because the entropy is extremely difficult to measure observationally, but the incident flux is easily calculated from stellar and orbital properties. To aide the reader, we represent fluxes as the corresponding equilibrium temperatures assuming zero albedo and full heat redistribution: $T_{\text{eq}}^4 = F/(4\sigma_b)$, where σ_b is the Stefan-Boltzmann constant.

Figure 7 shows the relationship between equilibrium temperature and entropy for planets with masses between 0.1 and 10 M_J in thermal equilibrium with T_{eq} between 1000 and 2500 K. For planet's within this range the entropy is interpolated with T_{eq} at a constant mass from the two T_{eq} -S curves with closest temperatures. More massive planets were considered by extrapolating

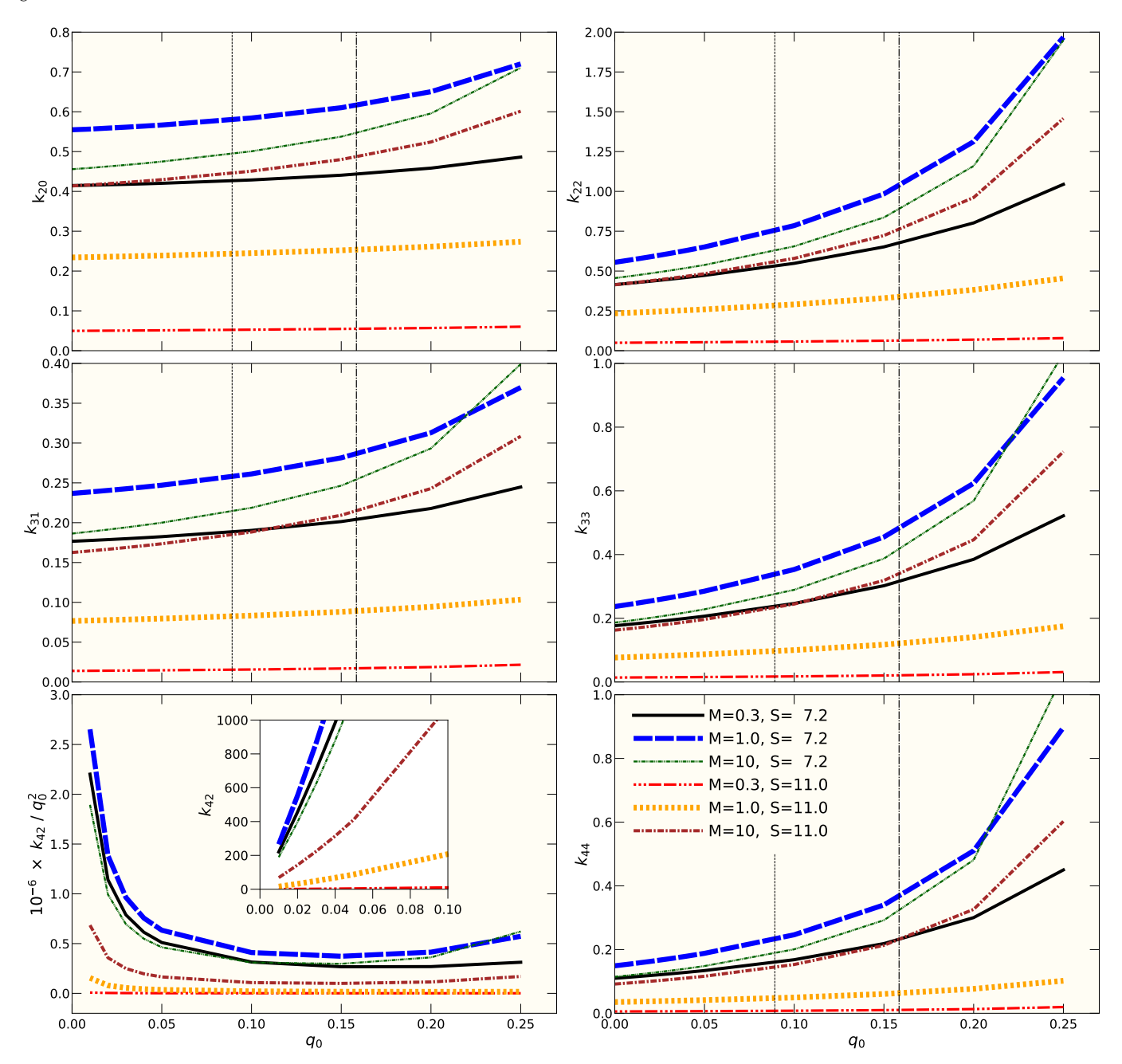


Figure 4. Tidal Love numbers, k_{nm} for six planet models are shown as function of q_0 . The masses and interior entropies are given in the legend of the lower right plot. In the lower left panel, k_{42} has be divided by q_0^2 while the inset show the original k_{42} . The vertical lines mark the q_e values of Jupiter and Saturn as in Fig. 3.

the T_{eq} -S curves as a function of $\log_{10}(M)$. Cooler planets were considered using a curve constant entropy of $S=7.2~k_B/{\rm el.}$, which is the condition for the onset of helium rain as shown in Figure 1. The temperature for this 'cold' curve is then defined by the reported effective temperatures for Jupiter and Saturn at the onset of helium rain by Mankovich & Fortney (2020). However, planets with lower incoming stellar energy flux are likely to be further from the assumed equilibrium state. Our relationship between specific entropy and T_{eq} relies

on a fit to the observed population of hot Jupiters (in Thorngren & Fortney 2018). As such, we have avoided extrapolating very far into regions of mass-flux space where few to no hot Jupiters are found. In general, this cutoff moves to higher masses as the temperature increases, as a result of planet formation processes outside the scope of this paper.

Statistical uncertainties in the heating efficiency from Thorngren & Fortney (2018) are approximately 0.5%, which leads to an uncertainty in the resulting $T_{\rm int}$ of

Name	t_{orbit} (days)	$R_{ m orbit}$ (AU)	e	$M_{ m p}$ $(M_{ m J})$	$R_{\rm p}$ $(R_{\rm J})$	$M_{ m st}$ (M_{\odot})	$R_{ m st}$ (R_{\odot})	$T_{\rm eff,st}$ (K)	$T_{\rm eq,p}$ (K)	S (k_B/e^-)
				/	,					
HAT-P-13b	2.916	0.04269	0.0133	0.851	1.272	1.22	1.56	5653	1649	11.14
WASP-18b	0.9415	0.02009	0.0091	10.40	1.191	1.22	1.23	6400	2416	10.92
WASP-4b	1.338	0.02261	0	1.186	1.321	0.86	0.89	5400	1634	10.99
WASP- $12b$	1.091	0.02338	0	1.465	1.937	1.43	1.66	6360	2585	11.87
WASP-121b	1.275	0.02544	0	1.183	1.865	1.35	1.46	6459	2361	11.84
WASP- $103b$	0.9255	0.01987	0	1.49	1.528	1.22	1.44	6110	2509	11.81
Kepler-75b	8.885	0.08164	0.57	10.1	1.05	0.91	0.89	5200	870	8.26
CoRoT-3b	4.257	0.05738	0	21.66	1.01	1.37	1.56	6740	1695	9.90

Table 2. Parameters for selected exoplanets. (a) Winn et al. (2010), (b) Shporer et al. (2019), (c) Bouma et al. (2019), (d) Chakrabarty & Sengupta (2019), (e) Delrez et al. (2016), (f) Gillon et al. (2014), (g) Bonomo et al. (2015), (h) Deleuil et al. (2008). All parameters from (NASA Exoplanet Science Institute 2011). $T_{\rm eq,p}$ assumes zero albedo. S interpolated from the relationships in Fig. 7.

around 35 K, varying with the incident flux. However, these statistical uncertainties are less significant than the modelling uncertainty, which is much more difficult to quantify. An alternate approach was presented by Sarkis et al. (2021) who found broadly similar values for the heating efficiency, though their peak heating of 2.5%was at a higher temperature of ~ 1860 K. Thorngren & Fortney (2018) found a peak of 2.5% at 1500 - 1600 K. This difference appears to be the result of differences in the atmosphere models. (Mollière et al. 2015) included the effects of TiO and VO species on upper atmosphere opacities, whereas Fortney et al. (2007) and therefore Thorngren & Fortney (2018) did not. Both papers are fitting to the observed radius via the entropy, so the difference in the predicted entropy for a given planet likely does not differ as much as the heating efficiency. However, this fit relies on assumptions for a planet's composition (abundance of helium and heavier elements) and the equation of states that defines isentropic paths in P-T space and the corresponding density. Uncertainties in the equation of state of hydrogen-helium mixtures and their impact on giant planet structure have been discussed by Saumon & Guillot (2004); Militzer et al. (2016); Helled et al. (2020)

The interior density profile is determined by the isentropic pressure-density curve derived from the equation of state, which depends both on the entropy and on the heavy element fraction of the envelope, Z. Given the observational constraints on mass and radius, a two-layer model exoplanet can accommodate heavy element mass in both the core and envelope. Figure 8 shows the density profiles of two end-member cases for each selected exoplanet. The first end-member is the case of a coreless model, which corresponds to a maximum value for Z in the envelope. The second case is a model in which Z=0 in the envelope, corresponding to a maximum core

mass. These are compared to two-layer analogue models of Jupiter and Saturn, which match the observed J_2 for each (Iess et al. 2019; Durante et al. 2020), in addition to the mass and radius. Two-layer models are known to do a poor job in reproducing the full gravitational field of Jupiter and Saturn, since they ignore the redistribution of helium, as well as a possible 'dilute' core (Wahl et al. 2017b; Mankovich & Fuller 2021) or inhomogeneity of Z across the helium rain layer (Miguel et al. 2016; Debras & Chabrier 2019). For this reason the two-layer analogues of Jupiter and Saturn have more massive central cores and require either negative values of Z or significantly higher temperatures than more complicated interior models. In Figure 8 there are evident influences from both planet mass and equilibrium temperature, with the very massive CoRoT-3b exhibiting the highest densities in the deep envelope, and the highly irradiated WASP-12b and WASP-121b exhibiting far more extended envelopes with notably lower density gradients in the outer portion of the planet.

As a consequence of their assumed tidally-locked state, both the tidal and rotational parameters, q_0 and $q_{\rm tid}$, are tied to the orbital distance of the planet. Table 3 presents q_0 and $q_{\rm tid}$ for the eight selected exoplanets in the assumed 1:1 resonance locked state, along with results from computed tidal responses, k_{22} and k_{20} , and shape for the two end-member interior structures. For the planet shape we report the three principle axes lengths: a, equatorial radius along the star-planet axis, b, equatorial radius perpendicular star-planet axis, and c, polar radius along the rotation axis. Additionally, we report the prolateness and oblateness, defined as

$$f_{ac} = \frac{a-c}{a}$$
 and $f_{bc} = \frac{b-c}{b}$, (9)

respectively. Although the aforementioned shape parameters are commonly used to describe triaxial ellip-

Planet name	$q_{ m rot}$	$q_{ m tid}$	Z	M_c $[M_{ m J}]$	R_c $[R_J]$	k_{22}	k_{20}	a [R _J]	b [R _J]	c [R _J]	f_{ac}	f_{bc}	ΔR	$C/(Ma_0^2)$
HAT-P-13b	4.06e-2	-0.0122	0.389	0	0	0.34	0.337	1.27600	1.26561	1.26223	1.08e-2	2.67e-3	6.39e-3	0.220
			0	0.387	0.232	0.0866	0.0862	1.27956	1.27103	1.26825	8.84e-3	2.18e-3	1.86e-3	0.108
WASP-18b	2.61e-2	-7.78e-2	0.212	0	0	0.424	0.422	1.19632	1.18967	1.18748	7.39e-3	1.84e-3	2.04e-3	0.240
			0	2.53	0.225	0.226	0.225	1.19595	1.19022	1.18832	6.38e-3	1.59e-3	1.45e-3	0.177
WASP-4b	0.0155	-0.0464	0.308	0	0	0.393	0.381	1.35600	1.31136	1.29796	4.28e-2	1.02e-2	1.25e-2	0.230
			0	0.409	0.227	0.139	0.136	1.35369	1.31667	1.30546	3.56e-2	8.51e-3	7.59e-3	0.137
WASP-121b	0.0481	-0.144	0.238	0	0	0.296	0.275	2.02633	1.82110	1.77207	0.125	2.69-2	3.82e-2	0.200
			0	0.313	0.228	0.122	0.115	2.03212	1.84487	1.79998	0.114	2.43e-2	2.34e-2	0.130
WASP-12b	0.0594	-0.178	0.19	0	0	0.332	0.304	2.16934	1.88228	1.82032	0.161	3.29e-2	4.64e-2	0.206
			0	0.294	0.223	0.165	0.154	2.17185	1.90686	1.84932	0.149	3.02e-2	3.15e-2	0.150
WASP-103b	0.0399	-0.119	0.347	0	0	0.388	0.362	1.64989	1.50378	1.46720	0.111	2.43e-2	2.87e-2	0.223
			0	0.589	0.237	0.109	0.104	1.63427	1.51422	1.48355	9.22e-2	2.03e-2	1.95e-2	0.117
Kepler-75b	2.07e-5	-6.15e-5	4.21e-3	0	0	0.447	0.447	1.04978	1.04973	1.04971	5.91e-5	1.52e-5	2.64e-4	0.246
			0	4.40e-2	7.11e-2	0.442	0.442	1.04987	1.04982	1.04981	6.00e-5	$1.52\mathrm{e}\text{-}5$	1.76e-4	0.244
CoRoT-3b	3.74e-5	-1.11e-4	8.32e-2	0	0	0.387	0.387	1.00894	1.00886	1.00883	1.02e-4	2.58e-5	1.14e-3	0.232
			0	2.30	0.178	0.301	0.301	1.00992	1.00984	1.00982	9.6e-5	$2.48\mathrm{e}\text{-}5$	1.67e-4	0.207

Table 3. Predictioned shape and tidal response for selected exoplanets assuming a tidally-locked state and a two-layer interior models with N = 1025 CMS layers. For every planet, the top line is for the fully-mixed case with no central core. The lower line corresponds to the fully separated case with envelope Z = 0 and maximum core mass.

soids, we note that the spheroidal surface predicted by CMS represents a more general shape. In fact, the calculated surface is only an exact ellipsoid in the case of a constant density planet (Wahl et al. 2017a).

HAT-P-13b and the five planets selected from the WASP catalog exhibit extremely short orbital periods, and are expected expected to be tidally locked. Kepler-75b and CoRoT-3b orbit much more distantly, leading to much smaller values of q_0 . For reasonable values of tidal quality factor, Q, the two more distantly orbiting plates are also likely to be tidally locked. Alternatively, if like Jupiter and Saturn, these planets rotatation rates have not been significantly slowed by tidal torques, then the values of q_0 could be orders of magnitude higher than for the tidally-locked state reported here.

For all eight exoplanets, the end-member interior structure case with Z=0 in the envelope determines the maximum core mass and radii, and corresponds to a minimum minimum prediction of, f_{ac} and f_{bc} , as well as minimal values in k_{20} and k_{22} . Conversely, the case with no central core yields the maximum Z in the envelope, as well as a maximum values for f_{ac} . f_{bc} , k_{22} , and k_{20} . While not explicitly considered here, planets with dilute cores (Wahl et al. 2017b) are expected to exhibit tidal responses between these two end-member cases, since they represent intermediate degree of concentration of heavy elements between a fully mixed planet, and one with all heavy elements in a dense, central core.

While the central concentration of heavy elements has the strongest influence on k_{22} for a given planet, the planet mass and equilibrium temperature are significant over the full parameter space of giant exoplanets. Figure 9 shows five mass-radius relationships calculated for two-layer models with a constant $10~M_{\oplus}$ core and Z=0

in the envelope, along with the corresponding k_{22} for a tidal response in the linear regime, $q_0 < 1 \times 10^{-5}$ and $q_{tid} > -1 \times 10^{-5}$. The blue curve shows the mass-radius relationship for "cold" exoplanets with $S = 7.2~k_{\rm B}/{\rm el}$. This shows the characteristic trend with radius first increasing with mass to a maximum of $\sim 1.05~R_{\rm J}$ at $\sim 3~M_{\rm J}$, and then decreasing as additional mass leads to a shrinking radius due to compaction of the the hydrogenhelium envelope. The calculated k_{22} follows a qualitatively similar trend with a 0.1 $M_{\rm J}$ planet exhibiting a k_{22} of ~ 0.2 and increasing with mass to a maximum at ~ 0.56 at $\sim 1.5~M_{\rm J}$, and then decreasing to ~ 0.46 at 10 $M_{\rm J}$.

The mass-radius relationship for a constant $T_{\rm eq}$ = 1000 K has a quite different appearance, with an inflated $0.1 M_{\rm J}$ planet first decreasing with mass, flattening out at $\sim 0.6 M_{\rm J}$, and then decreasing further for $M > 2 M_{\rm J}$. The slope at low masses becomes steeper with increasing T_{eq} , and the radius decreases monotonically, with an inflection point moving to higher masses for higher T_{eq} . Meanwhile, the calculated k_{22} decreases with increasing $T_{\rm eq}$, with the maximum k_{22} for a given mass-radius relationship shifting to higher masses. While increasing envelope Z leads to a decrease in radius, it has a somewhat less intuitive influence on k_{22} . For a colder Jupiter-mass planet with $S = 7.20 k_B/el.$, increasing Z leads to a very slight decrease in k_{22} , while an identical mass planet with $T_{\rm eq}$ = 2500 K exhibits a more substantial increase in k_{22} with Z.

The observed k_{22} values for exoplanets, summarized in Figure 6, cover a wider range of values, most of which are larger than our models can account for with a two-layer interior structure and static tidal response. The Hardy et al. (2017) observation of HAT-P-13b and the Bouma

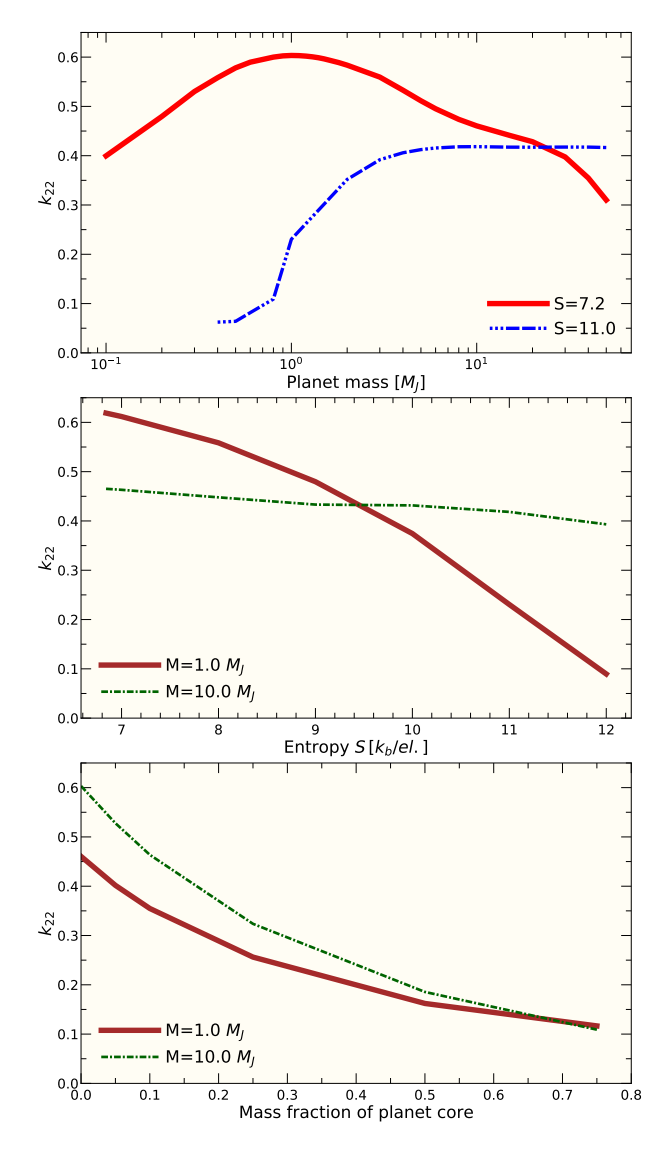


Figure 5. For slowly rotating planets, the three panels show the tidal coefficient k_{22} as a function of planet mass (top), the envelope entropy, S (middle), and core mass (bottom).

et al. (2019) observation of WASP-4b are both significantly larger than our model predictions, and even considering the reported uncertainties. They are, in fact, larger than the maximum of ~ 0.6 for any combination of parameters considered, with the possible exception of models undergoing extremely fast rotation. Our calculated range for WASP-18b has a maximum quite close to lower limit of their prediction with the reported uncertainty (Csizmadia et al. 2019). Given the uncertainties on exoplanet mass, radius and equilibrium temperature be observation may, therefore, be compatible with a static tidal response of a core-less planet, or one in which the core is a small fraction of the planet mass.

The observation of HAT-P-13b by (Buhler et al. 2016) is the only observation showing significant overlap with the range of k_{22} predicted here. Figure 10 demonstrates how Z, k_{22} , and f vary as a function of core mass for our models of HAT-P13b and WASP-121b. The k_{22} observed by Buhler et al. (2016), is consistent with a model planet ranging from no core to $\sim 0.075~M_{\rm J}~(\sim 24$ M_{\oplus}) and Z between $\sim 0.34 - 0.39$. It would, therefore, suggest that HAT-P-13b has both a more massive core and an envelope more enriched in heavy elements than Jupiter (Miguel et al. 2016; Wahl et al. 2017b). The magnitudes of the proplateness and oblateness are governed primarily by q_0 and $q_{\rm tid}$, but both shows 18% decrease between the fully mixed and fully separated HAT-P-13b models. The hotter, more expanded WASP-121b exhibits qualitatively similar dependence on M_c , but with the observed mass and radius permitting a narrower range of Z and M_c , and consequently, a smaller range of k_{22} .

In the linear regime, the static tidal response is fully determined by the density profile, and $k_{22} = k_{20}$ (Wahl et al. 2017a). Figure 11 demonstrates that the simulations for the various mass-radii relationships, calculated with low q_0 and $q_{\rm tid}$ precisely follow the relationship $k_{22} = 3J_2/q_0$. For larger values of q_0 and $q_{\rm tid}$, nonlinearity in the tidal response leads to splitting between the Love numbers k_{22} and k_{20} . Jupiter and Saturn are in a regime with $q_0 \gg q_{\rm tid}$ and exhibit significant deviation form the linear regime relationship (Lainey et al. 2017, 2020; Wahl et al. 2017a; Durante et al. 2020; Wahl et al. 2020). For hot Jupiters, q_0 is limited to be of similar order of magnitude as $q_{\rm tid}$ due to tidal locking, which means that significant deviations from the linear relationship occur only in the most extreme cases. Of the selected exoplanets, WASP-12b, WASP-103b, WASP-121b all have k_{22} values enhanced by over 10% from $3J_2/q_0$, with WASP-4b a slightly lesser $\sim 8\%$ deviation. The largest deviation of $\sim 19\%$ is found for a core-less WASP-12 model. Thus we find that in the most extreme cases, tidally-locked hot Jupiters can exhibit appreciably non-linear tidal responses, though still to a lesser extent than the faster rotating solar system giants. Conversely, non-linearities can be safely ignored for exoplanets with $q_0 \ll 0.01$.

Figure 12 shows influence of q_0 on the second-order Love numbers, k_{22} and k_{20} , while maintaining $q_{\rm tid}$ at the value in Table 2 for the HAT-P-13b and WASP-121b models. As q_0 is increased, k_{22} and k_{20} split from their initial degenerate state. While this suggests that an observed k_{22} as large Hardy et al. (2017) might be possible for static tidal response of a planet of HAT-P-13b's interior parameters, it would a require $q_0 \sim 0.2$, roughly two

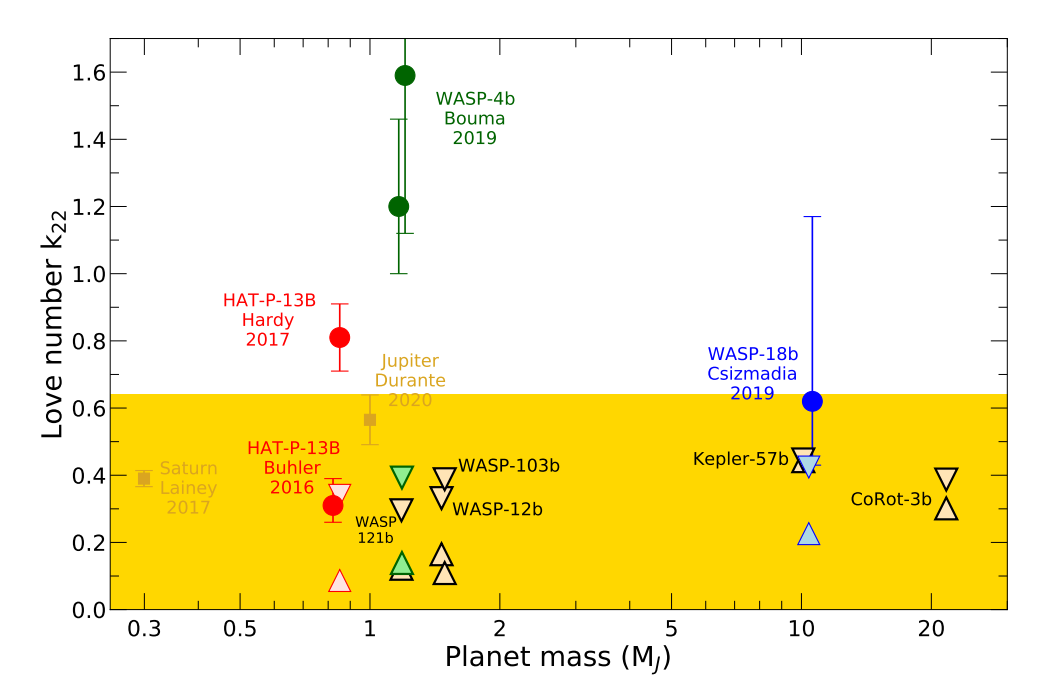


Figure 6. The triangles show the calculated limits on k_{22} for the selected exoplanets in Table 2. The upper limit is a model without a central core, while the lower limit is a case with no heavy elements in the envelope (Z=0). The filled circles represent exoplanets with reported k_{22} observations. The shaded region represents values of $k_{22} \le 0.6$ that can be explained in terms of a static tidal response.

orders of magnitude larger than for the tidally-locked state. Figure 13 considers the complimentary exercise of raising the magnitude of $q_{\rm tid}$ while maintaining q_0 . In this case the degree of splitting of k_{22} and k_{20} remains similar, while the overall of magnitude increase at large magnitudes of $q_{\rm tid}$. In both cases both q_0 and $q_{\rm tid}$ exhibit a comparable effect on the deviation from the linear regime response, but nonlinear response accounting for $\sim 16\%$ of WASP-121b's k_{22} , but < 2% for HAT-P-13b.

When a tidally locked planet transits, the star's flux is dimmed by a disk of radius \sqrt{bc} . Leconte et al. (2011) compared this value to the radius of nonrotating, unperturbed planet, a_0 , and introduced the radius correction factor,

$$\Delta R = \frac{a_0 - \sqrt{bc}}{\sqrt{bc}} \quad . \tag{10}$$

For WASP-12b, the largest correction in their dataset, they obtained a ΔR range of 0.025–0.035. When we use the same planet parameters, we find reasonable agreement with this correction despite the fact that Leconte et al. (2011) based their work on the theory of figures while we use the nonperturbative CMS theory here. They represented the interiors of hot Jupiters with a polytropic EOS while we used a more realistic EOS for hydrogen-helium-Z mixtures that was derived from ab initio computer simulations and yielded models for Jupiter and Saturn that agreed well with spacecraft ob-

servations (Iess et al. 2018; Wahl et al. 2017b). When we calculated ΔR for WASP-12b for $M=1.465\,M_J$ and $a_0=1.937\,R_J$, we obtained $\Delta R=0.0340$ for models with $M_c=0.293\,M_J$ and Z=0 and $\Delta R=0.0481$ for $M_c=0$ and Z=0.19. However, when we adopt the earlier parameters for WASP-12b, $M=1.404\,M_J$ and $a_0=1.736\,R_J$, we respectively obtain $\Delta R=0.0220$ and 0.0330 for our models with and without a core, a difference of only $\sim 6\%$ from Leconte et al. (2011). In general one finds that giant planets with large cores respond less of tidal perturbations and thus their transit radius correction is smaller.

Akinsanmi et al. (2019) investigated how many transit observations with current instruments would be needed to determine the Love number of WASP-103b. They adopted a very wide range of shape Love number, h_{22} , ranging from 0.0 to 2.5 (For fluid planets, $h_{22} = 1 + k_{22}$ holds.) Based on our interior models, we predict a much narrower range for this planet with k_{22} values between 0.109 and 0.388 depending on whether planet has core of 0.588 M_J or no core at all.

Correia (2014) assumed $k_{22} = 0.5$ and studied the shape and light curves for a number of exoplanets. Hellard et al. (2019) investigated how k_{22} can be derived from the transit light curves and constructed models for the shape of exoplanets under very specific assumptions. Qualitatively our results for WASP 4b, 12b and 18b in Tab. 3 agree with these model predictions but one also

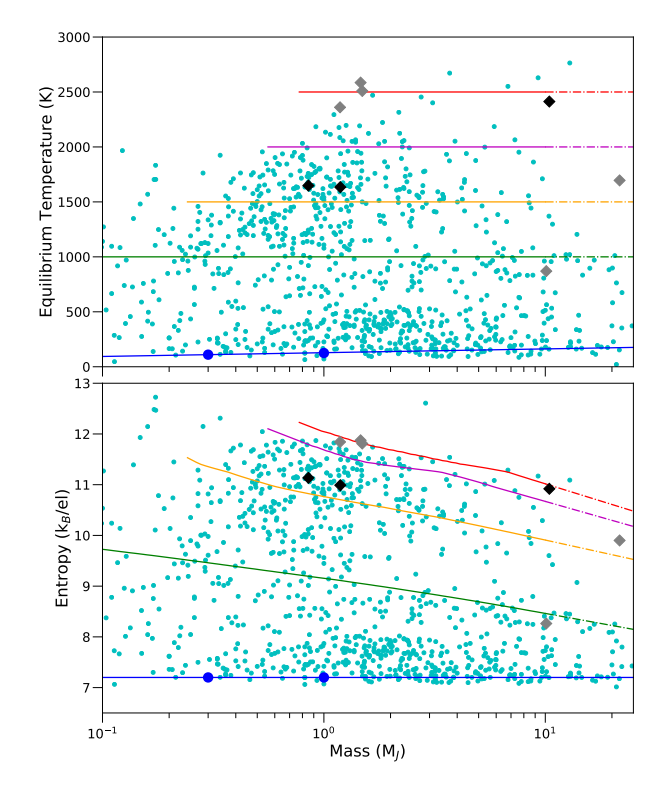


Figure 7. Equilibrium temperature (top) and entropy (bottom) relationship calculated for thermal equilibrium as a function of planet mass shown as solid lines at $T_{\rm eq}=1000$, 1500, 2000, and 2500 K. Extrapolated $T_{\rm eq}$ -S trends for planet masses $> 10~M_{\rm J}$ shown with dash-dotted lines. Condition for the onset of helium rain in Saturn and Jupiter denoted by blue circles. Diamonds are selected exoplanets in Tab. 2 with published k_2 observations (black) and without (gray). Planets in (NASA Exoplanet Science Institute 2011) with the necessary parameters are shown in cyan under the same assumptions of thermal equilibrium.

notices some deviations. Correia (2014) predicted much larger values for the flattenings f_{ac} and f_{bc} of WASP-18b because they used a larger planet radius of 1.52 R_J , while we used 1.191 R_J . Although we derived a k_{22} range from 0.226 to 0.424 rather than setting it to 0.5. Our predictions for WASP-18b agree fairly well Hellard et al. (2019) with only a small deviation for f_{ac} ; they derived 0.0077, which is slightly outside of our range of 0.0064–0.0074.

For WASP-4b, the predictions by Hellard et al. (2019) for f_{ab} , f_{bc} , and f_{ac} are all found to be slightly outside the range that is spanned by our models with and without cores. For example, we determined $f_{ac} = 0.036-0.043$ while they predicted 0.045.

For WASP-12b, we find better agreement with the shapes predicted by Correia (2014) once we adopted the older planet radius. However, even in this case their

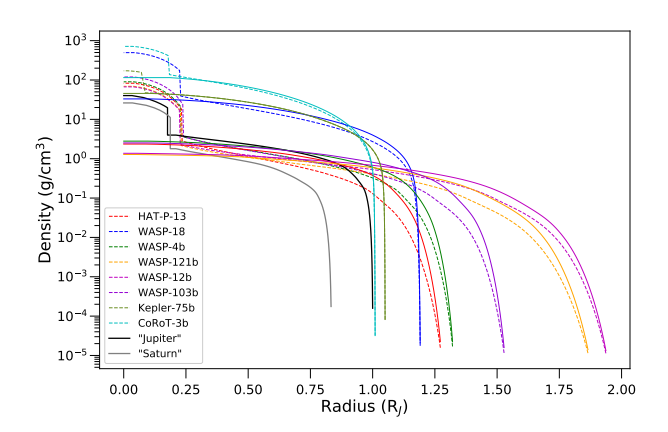


Figure 8. Density as a function of radius from the center of the planet for eight exoplanets and analogue Jupiter and Saturn. For each exoplanet, two end-member interior structures are shown: (solid) fully mixed with no core and maximum envelope Z, and (dashed) fully separated with maximum core mass and envelope Z=0. Saturn and Jupiter analogues have M_c and Z chosen to match the observed J_2 (Iess et al. 2019; Durante et al. 2020).

 f_{bc} =0.031 and that of Hellard et al. (2019), 0.036, are above of our predicted range of 0.023–0.026 by $\sim 20\%$.

Hellard et al. (2020) reported a tentative measurement of WASP-121b Love number, $h_{22} = 1.39^{+0.71}_{-0.81}$, which is compatible with the range of $h_{22} - 1 = k_{22} = 0.122$ to 0.296, but not well constrained given the large reported uncertainty.

It is worth noting that in all cases summarized above, once parameters were selected to best match the previous estimates, that our models consistently predict values of f_{ac} , f_{bc} and ΔR slightly below the reported values. This suggests a systematic overestimation of the flattening by these models, possibly resulting from a less realistic hydrogen-helium equation of state, neglecting non-linear effects or artificially or constraining the surface shape to an perfect ellipsoid.

4. CONCLUSIONS

We studied the tidal response and shape of hot Jupiters, identified a number of general trends, and modeled eight specific exoplanets. Most tidally locked exoplanets are slowly rotating. They are thus in the linear regime, for which Love number is well approximated by $k_{22} = 3J_2/q_0$ and cannot be greater than 0.6. This limit was derived under realistic assumptions for giant planet interiors in which the density strongly varies throughout the envelope. For close-in hot Jupiters, we studies how the high interior temperatures reduce the density profile of the envelope and demonstrate that this change further reduces k_{22} .

We also studied how the tidal response changes with increasing rotation rate. For extremely close-in hot

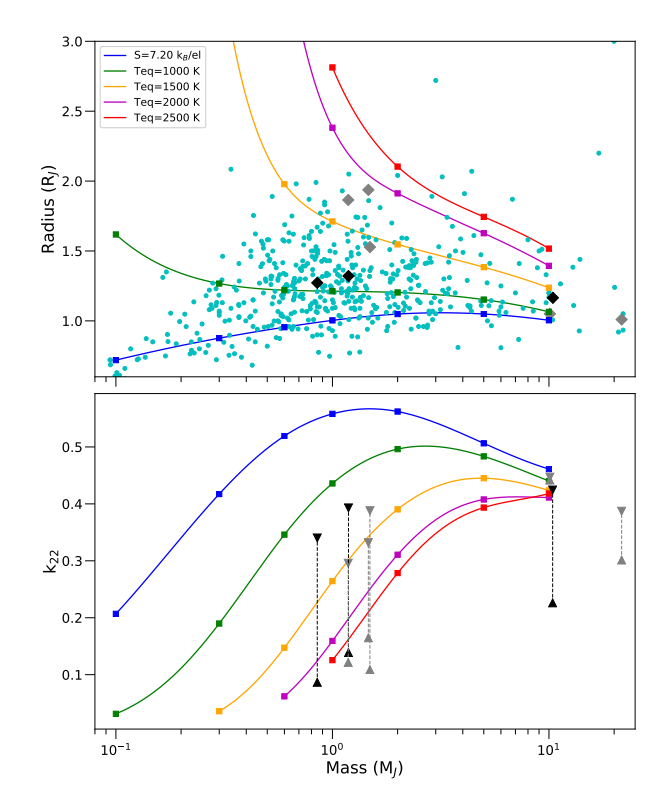


Figure 9. (Top) mass-radius relationship for two-layer interior models with $M_c=10~M_{\oplus},Z=0$ and constant $T_{\rm eq}$ between 1000 and 2500 K (red, magenta, yellow, green squares) and for a constant entropy $S=7.2~k_B/{\rm el.}$ (blue squares). Shown for comparison are masses and radii of confirmed exoplanets (cyan circles) (NASA Exoplanet Science Institute 2011) and selected exoplanets (black and gray diamonds). (Bottom) corresponding Love number, k_{22} , for mass-radius curves. Predicted range of k_{22} for selected exoplanets shown as in Fig. 6.

Jupiters, we find that, in spite of tidal locking, rotation rates are sufficient to have a noticeable effect tidal response. For three of the selected exoplanets, WASP-12b, WASP-103b and WASP-121b, we predict k_{22} to exceed the linear value of $k_{22}=3J_2/q_0$ by over 10%, with the largest deviation of $\sim 19\%$ for WASP-12.

For realistic planet and stellar parameters, we find $k_{22} < 0.45$ for all eight selected exoplanets. This limit is not compatible with much larger k_{22} values that have been reported in the literature of number of hot Jupiters (Hardy et al. 2017; Bouma et al. 2019; Csizmadia et al. 2019), which may indicate a systematic overestimation of k_{22} by these observation methods. Only the observation of HAT-P-13b by Buhler et al. (2016) overlaps with our predicted k_{22} range.

If the larger k_{22} observations are confirmed, they imply that these planets are either fast rotating and thus not tidally locked, or that dynamic tidal effects increase k_{22} in ways that are not understood. For Jupiter, how-

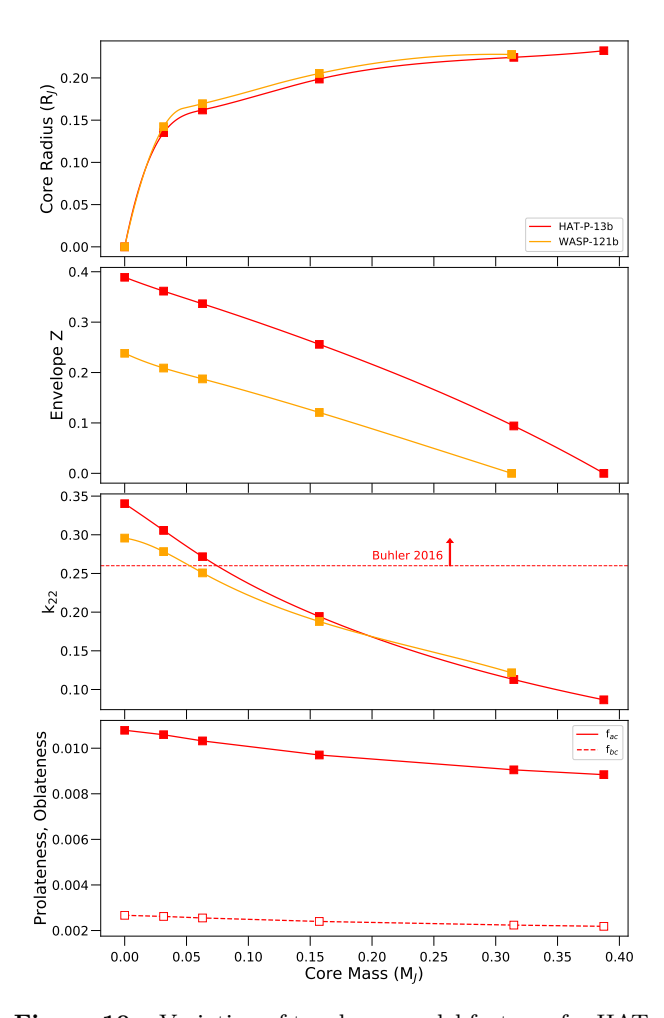


Figure 10. Variation of two-layer model features for HAT-P-13b and WASP-121b with core mass. (Top panel) Core radius, (second panel) heavy element fraction, Z, of the envelope, (third panel) Love number, k22, (bottom) prolateness, f_{ac} (solid) and oblateness, f_{bc} (dashed). The horizontal line in panel 3 shows the minimum value consistent with the observed k_{22} from Buhler et al. (2016).

ever, dynamic contributions to the tidal response (Idini & Stevenson 2021; Lai 2021) have been shown to reduce the static value (Wahl et al. 2020) by approximately $\Delta k_{22}/k_{22}^{\rm static} \approx 4\%$ bringing it in agreement with observations made by the *Juno* spacecraft (Durante et al. 2020). For dynamic tidal effects to explain the discrepancy between the large observed values and our model predictions, they would not only have to have the opposite sign as for Jupiter but also be much larger in magnitude.

We compare our predictions for the shape of selected planets with earlier models by Leconte et al. (2011); Correia (2014); Akinsanmi et al. (2019); Hellard et al. (2019) that relied on perturbative approaches and simpler assumptions for planetary interiors. Although we

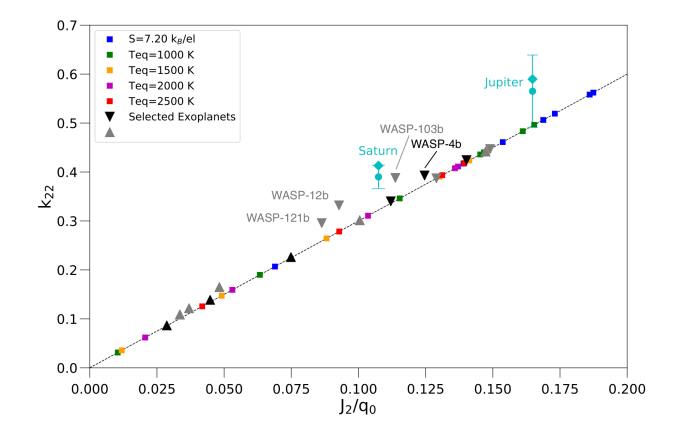


Figure 11. Comparison of the tidal response to the expected linear-regime response. Dotted black line shows the relation $k_{22}=3J_2/q_0$. Colored squares show results from the mass-radius curves and, triangles show results for the selected exoplanets following the same notation as Figure 9. Cyan circles and diamond show the observed (Lainey et al. 2017; Durante et al. 2020) and calculated (Wahl et al. 2017a, 2020) static k_{22} for Jupiter and Saturn for comparison. Also labeled are the four exoplanet models with the largest non-linearities.

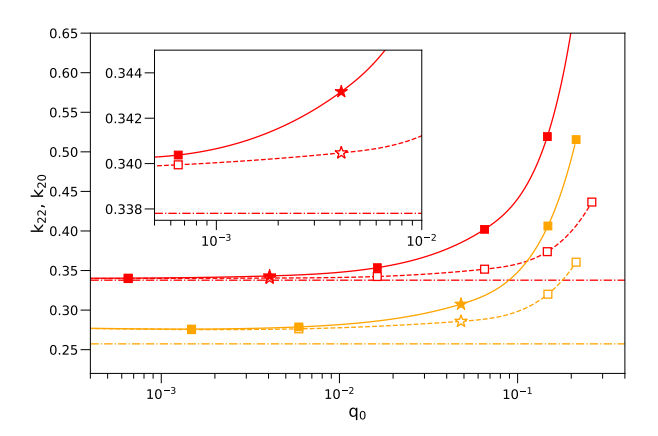


Figure 12. Variation of second-order Love numbers k_{22} and k_{20} with magnitude of rotational parameter q_0 . Red curves are are for HAT-P-13b, yellow for WASP-121b. k_{22} is a solid curve with filled squares, k_{20} dashed with open squares. k_{2m} for the tidally-locked state with the observed orbital period is denoted with stars. For each planet the linear-regime tidal response of $3J_2/q_0$ is shown with a dash dot. Simulations for this figure use fewer ($N_l = 128$) CMS layers.

find reasonably good agreement for the shape and the transit radius correction if we assume the same masses and radii as the other authors, we also suggest these models may have a small but systematic overestimation of the planet's flattening.

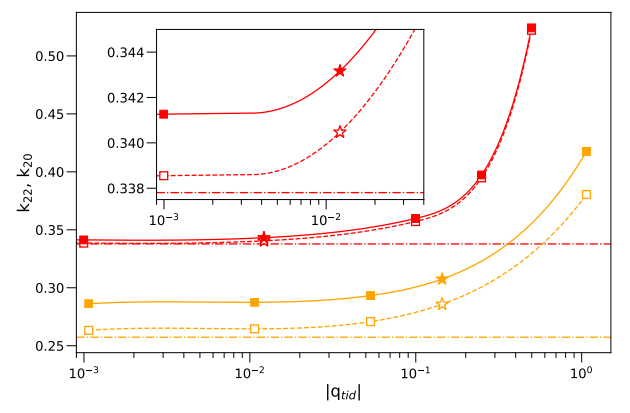


Figure 13. Variation of second-order Love numbers k_{22} and k_{20} with magnitude of tidal parameter $q_{\rm tid}$. Quantities are depicted the same as in Figure 12. Simulations for this figure use fewer ($N_l = 128$) CMS layers.

ACKNOWLEDGEMENTS

- This work was in part supported by the NASA mission
- ² Juno. BM acknowledges support from the Center for
- Matter at Atomic Pressure (CMAP) that is funded by
- 4 the U.S. National Science Foundation (PHY-2020249).
- 5 DT acknowledges support by the Trottier Fellowship
- from the Exoplanet Research Institute (iREx). This re-
- search has made use of the NASA Exoplanet Archive
- 8 and data provided by the WASP consortium.

REFERENCES

- Akinsanmi, B., Barros, S. C., Santos, N. C., et al. 2019, Astron. Astrophys., 621, A117
- Batygin, K., Bodenheimer, P., & Laughlin, G. 2009, Astrophysical Journal, 704, 49, doi: 10.1088/0004-637X/704/1/L49
- Becker, A., Bethkenhagen, M., Kellermann, C., Wicht, J., & Redmer, R. 2018, The Astronomical Journal, 156, 149, doi: 10.3847/1538-3881/aad735
- Becker, A., Lorenzen, W., Fortney, J. J., et al. 2015, Astrophysical Journal, Supplement Series, 215, doi: 10.1088/0067-0049/215/2/21
- Bonomo, A. S., Sozzetti, A., Santerne, A., et al. 2015, A&A, 575, A85, doi: 10.1051/0004-6361/201323042
- Bouma, L. G., Winn, J. N., Baxter, C., et al. 2019, The Astronomical Journal, 157, 217,doi: 10.3847/1538-3881/ab189f
- Buhler, P., Knutson, H., Batygin, K., et al. 2016, The Astrophysical Journal, 821, 26,doi: 10.3847/0004-637X/821/1/26
- Burton, J. R., Watson, C. A., Fitzsimmons, A., et al. 2014, Astrophysical Journal, 789, doi: 10.1088/0004-637X/789/2/113
- Campo, C. J., Harrington, J., Hardy, R. A., et al. 2011, Astrophysical Journal, 727, doi: 10.1088/0004-637X/727/2/125
- Chabrier, G., Mazevet, S., & Soubiran, F. 2019, ApJ, 872, 51
- Chakrabarty, A., & Sengupta, S. 2019, AJ, 158, 39, doi: 10.3847/1538-3881/ab24dd
- Charbonneau, D., Brown, T. M., Latham, D. W., & Mayor, M. 2000, The Astrophysical Journal, 529, L45, doi: 10.1086/312457
- Correia, A. C. 2014, Astronomy and Astrophysics, 570, 1, doi: 10.1051/0004-6361/201424733
- Correia, A. C. M., & Rodríguez, A. 2013, The Astrophysical Journal, 767, 128, doi: 10.1088/0004-637X/767/2/128
- Csizmadia, S., Hellard, H., & Smith, A. M. 2019, Astronomy and Astrophysics, 623, 1, doi: 10.1051/0004-6361/201834376
- Debras, F., & Chabrier, G. 2019, The Astrophysical Journal, 872, 100, doi: 10.3847/1538-4357/aaff65
- Deleuil, M., Deeg, H. J., Alonso, R., et al. 2008, A&A, 491, 889, doi: 10.1051/0004-6361:200810625
- Delrez, L., Santerne, A., Almenara, J. M., et al. 2016, MNRAS, 458, 4025, doi: 10.1093/mnras/stw522
- Demory, B.-O., & Seager, S. 2011, ApJS, 197, 12, doi: 10.1088/0067-0049/197/1/12

- Durante, D., Parisi, M., Serra, D., et al. 2020,Geophys. Res. Lett., 47, e86572,doi: 10.1029/2019GL086572
- Folkner, W. M., Iess, L., Anderson, J. D., et al. 2017, Geophys. Res. Lett., 44, 4694, doi: 10.1002/2017GL073140
- Fortney, J. J., Glenzer, S. H., Koenig, M., et al. 2009, Phys. Plasmas, 16, 041003
- Fortney, J. J., Marley, M. S., & Barnes, J. W. 2007, ApJ, 659, 1661, doi: 10.1086/512120
- Gavrilov, S. V., & Zharkov, V. N. 1977, Icarus, 32, 443, doi: 10.1016/0019-1035(77)90015-X
- Gillon, M., Anderson, D. R., Collier-Cameron, A., et al. 2014, A&A, 562, L3, doi: 10.1051/0004-6361/201323014
- Guillot, T., & Showman, A. P. 2002, Astron. Astrophys., 385, 156, doi: 10.1051/0004-6361
- H., A. R., & Jeans, J. H. 1920, The Geographical Journal, 56, 69, doi: 10.2307/1781302
- Hardy, R. A., Harrington, J., Hardin, M. R., et al. 2017,
 The Astrophysical Journal, 836, 1,
 doi: 10.3847/1538-4357/836/1/143
- Hellard, H., Csizmadia, S., Padovan, S., Sohl, F., & Rauer,
 H. 2020, The Astrophysical Journal, 889, 66,
 doi: 10.3847/1538-4357/ab616e
- Hellard, H., Csizmadia, S., Spohn, T., & Breuer, D. 2019,The Astrophysical Journal, 878, 119,doi: 10.3847/1538-4357/ab2048
- Helled, R., Mazzola, G., & Redmer, R. 2020, Nature Reviews Physics, 2, 562
- Henry, G. W., Marcy, G. W., Butler, R. P., & Vogt, S. S. 2000, The Astrophysical Journal, 529, L41, doi: 10.1086/312458
- Hubbard, W. B. 2013, Astrophys. J., 768, 43, doi: 10.1088/0004-637X/768/1/43
- Hubbard, W. B., & Militzer, B. 2016a, Astrophys. J., 820. https://arxiv.org/abs/1602.05143
- —. 2016b. https://arxiv.org/abs/1602.05143
- Idini, B., & Stevenson, D. J. 2021. https://arxiv.org/abs/2102.09072
- Iess, L., Folkner, W. M., Durante, D., et al. 2018, Nature, 555, 220, doi: 10.1038/nature25776
- Iess, L., Militzer, B., Kaspi, Y., et al. 2019, Science, 2965, eaat2965, doi: 10.1126/science.aat2965
- Jackson, B., Greenberg, R., & Barnes, R. 2008, The Astrophysical Journal, 678, 1396, doi: 10.1086/529187
- Kellermann, C., Becker, A., & Redmer, R. 2018, Astronomy & Astrophysics, 615, A39,
 - doi: 10.1051/0004-6361/201731775

- Kramm, U., Nettelmann, N., Fortney, J. J., Neuhäuser, R., & Redmer, R. 2012, Astronomy and Astrophysics, 538, 1, doi: 10.1051/0004-6361/201118141
- Lai, D. 2021. https://arxiv.org/abs/2103.06186
- Lainey, V., Jacobson, R. A., Tajeddine, R., et al. 2017, Icarus, 281, 286, doi: 10.1016/j.icarus.2016.07.014
- Lainey, V., Casajus, L. G., Fuller, J., et al. 2020, Nature Astronomy, 4, 1053
- Leconte, J., Lai, D., & Chabrier, G. 2011, Astronomy and Astrophysics, 528, doi: 10.1051/0004-6361/201015811
- Lin, D. N., & Gu, P. G. 2004, Revista Mexicana de Astronomia y Astrofisica: Serie de Conferencias, 22, 95
- Lodders, K. 2010, in Formation and Evolution of Exoplanets, ed. R. Barnes (Wiley), 157–186, arXiv:0910.0811
- Love, A. E. H. 1909, Proceedings of the Royal Society of London. Series A, Containing Papers of a Mathematical and Physical Character, 82, 73, doi: 10.1098/rspa.1909.0008
- Mankovich, C. R., & Fortney, J. J. 2020, ApJ, 889, 51, doi: 10.3847/1538-4357/ab6210
- Mankovich, C. R., & Fuller, J. 2021, Nature Astronomy, 0, 0
 Miguel, Y., Guillot, T., & Fayon, L. 2016, Astron.
 Astrophys., 114, 1, doi: 10.1051/0004-6361/201629732
- Militzer, B., & Hubbard, W. B. 2013, ApJ, 774, 148, doi: 10.1088/0004-637X/774/2/148
- Militzer, B., Soubiran, F., Wahl, S. M., & Hubbard, W. 2016, Journal of Geophysical Research: Planets, 121, 1552, doi: 10.1002/2016JE005080
- Militzer, B., Wahl, S., & Hubbard, W. 2019, ApJ, 879, 78
 Miller, N., & Fortney, J. J. 2011, ApJL, 736, L29, doi: 10.1088/2041-8205/736/2/L29
- Mollière, P., van Boekel, R., Dullemond, C., Henning, T., & Mordasini, C. 2015, ApJ, 813, 47, doi: 10.1088/0004-637X/813/1/47
- Morales, M. A., Pierleoni, C., Schwegler, E., & Ceperley, D. M. 2010, Proc. Nat. Acad. Sci., 107, 12799
- NASA Exoplanet Science Institute. 2011, NASA Exoplanet Archive, doi: 10.26133/NEA1
- Nettelmann, N. 2019, The Astrophysical Journal, 874, 156, doi: 10.3847/1538-4357/ab0c03
- Padovan, S., Spohn, T., Baumeister, P., et al. 2018, Astron. Astrophys., 620, A178, doi: 10.1051/0004-6361/201834181

- Ragozzine, D., & Wolf, A. S. 2009, Astrophysical Journal, 698, 1778, doi: 10.1088/0004-637X/698/2/1778
- Sarkis, P., Mordasini, C., Henning, T., Marleau, G. D., & Mollière, P. 2021, A&A, 645, A79, doi: 10.1051/0004-6361/202038361
- Saumon, D., Chabrier, G., & Horn, H. M. V. 1995a, Astrophys. J. Suppl., 99, 713
- Saumon, D., Chabrier, G., & van Horn, H. M. 1995b, ApJSS, 99, 713
- Saumon, D., & Guillot, T. 2004, Astrophys. J., 609, 1170Seager, S., & Hui, L. 2002, The Astrophysical Journal, 574, 1004, doi: 10.1086/340994
- Seager, S., Kuchner, M., Hier-Majumder, C. A., & Militzer, B. 2007, ApJ, 669, 1279, doi: 10.1086/521346
- Shporer, A., Wong, I., Huang, C. X., et al. 2019, AJ, 157, 178, doi: 10.3847/1538-3881/ab0f96
- Thorngren, D., Gao, P., & Fortney, J. J. 2019, ApJL, 884, L6, doi: 10.3847/2041-8213/ab43d0
- Thorngren, D. P., & Fortney, J. J. 2018, The Astronomical Journal, 155, 214, doi: 10.3847/1538-3881/aaba13
- Vorberger, J., Gericke, D. O., Bornath, T., & Schlanges, M. 2010, Phys. Rev. E, 81, 046404
- Wahl, S. M., Hubbard, W. B., & Militzer, B. 2016, The Astrophysical Journal, 831, 14,doi: 10.3847/0004-637X/831/1/14
- —. 2017a, Icarus, 282, 183, doi: 10.1016/j.icarus.2016.09.011
 Wahl, S. M., Parisi, M., Folkner, W. M., Hubbard, W. B.,
 & Militzer, B. 2020, Astrophysical Journal, 891, 15,
 doi: 10.3847/1538-4357/ab6cf9
- Wahl, S. M., Hubbard, W. B., Militzer, B., et al. 2017b, Geophys. Res. Lett., 44, 4649, doi: 10.1002/2017GL073160
- Wilson, H. F., & Militzer, B. 2014, Astrophys. J., 973, 34
 Winn, J. N., Johnson, J. A., Howard, A. W., et al. 2010, ApJ, 718, 575, doi: 10.1088/0004-637X/718/1/575
- Zharkov, V. N. 2004, Astronomy Letters, 30, 496, doi: 10.1134/1.1774402
- Zharkov, V. N., & Gudkova, T. V. 2010, Planetary and Space Science, 58, 1381, doi: 10.1016/j.pss.2010.06.004
- Zharkov, V. N., & Trubitsyn, V. P. 1978, The physics of planetary interiors, ed. W. B. Hubbard (Tucson, AZ: Parchart), 380